Urban Climate 43 (2022) 101135

Contents lists available at ScienceDirect

Urban Climate

journal homepage: www.elsevier.com/locate/uclim

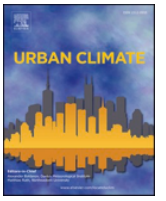

A dark target Kalman filter algorithm for aerosol property retrievals in urban environment using multispectral images

Gemine Vivone [a], Alberto Arienzo [c], Muhammad Bilal [d], Andrea Garzelli [e], Gelsomina Pappalardo [a], Simone Lolli [a,b,*]

[a] Italian National Research Council - Institute of Methodologies for Environmental Analysis (CNR-IMAA), Tito Scalo I-85050, Italy
[b] Kent State University (Florence Campus), E Summit St., Kent, OH 44240, USA
[c] University of Florence, Department of Information Engineering, Florence I-50139, Italy
[d] Nanjing University, Department of Information Science and Technology, Nanjing 210044, China
[e] University of Siena, Department of Information Engineering and Mathematics, Siena I-53100, Italy

ARTICLE INFO

Keywords:
Aerosol optical depth
Dark target
Kalman filter
Extended Kalman filter
Landsat
Remote sensing

ABSTRACT

Natural and anthropogenic aerosol atmospheric emissions play a fundamental role in directly modulating the incoming solar radiation and affecting the air quality, especially in large metropolitan regions. Likewise, aerosols indirectly impact cloud lifetime, atmospheric column thermodynamics and precipitation patterns. For these reasons, it is of particular importance to assess the aerosol spatial and temporal variability in the first instance to reduce the associated global climate models uncertainty to correctly forecasting future scenarios and then to react fast in applying mitigation strategies. In this paper, an aerosol optical depth (AOD) retrieval algorithm for high-spatial resolution images in the blue wavelength range for urban environments is developed for the first time. The proposed approach is completely blind because does not use look-up-tables or complex radiative transfer models, which require the setting/estimation of many parameters. The multi-wavelength (exploiting the coastal and the blue bands) AOD retrieval permits to retrieve also important aerosol micro-physical properties, e.g., the size. The proposed method leverages on the use of Kalman filters to deal with the unavoidable sensor's noise improving the accuracy of the estimation of the AOD. The approach is assessed on four different test cases acquired by Landsat 8 involving two metropolitan areas. A strong agreement to ground-based AERONET measurements is observed on several performance metrics. Clear advantages in comparison with the baseline approach relied upon the simple inversion of the explored model are pointed out.

1. Introduction

The Aerosol Optical Depth (AOD) is a comprehensive variable accounting for aerosol (natural or anthropogenic) optical and micro-physical properties widely used to assess the aerosol-cloud interactions (Mülmenstädt and Feingold, 2018), e.g. cloud formation, cloud lifetime, atmospheric column heating/cooling, which drastically influences the Earth-Atmosphere global radiative budget and then

* Corresponding author.
E-mail addresses: gemine.vivone@imaa.cnr.it (G. Vivone), alberto.arienzo@unifi.it (A. Arienzo), muhammad.bilal@connect.polyu.hk (M. Bilal), andrea.garzelli@unisi.it (A. Garzelli), gelsomina.pappalardo@imaa.cnr.it (G. Pappalardo), simone.lolli@imaa.cnr.it (S. Lolli).

https://doi.org/10.1016/j.uclim.2022.101135
Received 16 September 2021; Received in revised form 14 January 2022; Accepted 13 February 2022

climate. Further, the AOD, quantifying the extinction of solar radiation along the atmospheric column, can be used as proxy to estimate the particulate matter with an aerodynamic diameter $\leq 2.5\ \mu g$ (PM2.5) (Van Donkelaar et al., 2006; Toth et al., 2019). A poor air quality, with elevated concentrations of PM2.5 at surface, translates into increased mortality and morbidity due to cardiovascular disease (Miller et al., 2007) and lung cancer (Lepeule et al., 2012; Chudnovsky et al., 2014) especially in underdeveloped regions (Lolli et al., 2019). Recently, several studies relate PM2.5 also with an increase in COVID-19 pandemic transmission (Lolli and Vivone, 2020; Lolli et al., 2020) and a decrease in solar energy production (Lolli, 2021). Since the last decade, the European Union (EU) legislation put limitations on road transportation, domestic combustion and agriculture emissions. In the United States, the Environment Protection Agency (EPA) successfully implemented similar restrictions to limit anthropogenic emissions to improve the air quality, as showed in (Tosca et al., 2017). However, to fully understand aerosol-cloud interaction and to improve air-quality in large metropolitan areas, AOD observations at global and micro spatial scale are still needed, as well as at regional and urban scale (Mülmenstädt and Feingold, 2018; Chudnovsky et al., 2014). Currently, punctual high precision AOD measurements are provided by the National Aeronautic and Space Administration (NASA) AErosol RObotic NETwork (https://aeronet.gsfc.nasa.govAERONET; (Holben et al., 1998)), a global network of 1000+ permanent worldwide observation sites constituted by homogeneous sunphotometers retrieving daytime AOD with a temporal resolution of 60 s. However, the network, even if dense, struggles to characterize AOD variability both at regional and urban scale. For these reasons, in the last decades, scientific developments were encouraged to improve the AOD retrieval algorithms from multi-sensor multi-spectral instruments aboard satellites. The first satellite-based AOD estimation was possible just over dark surfaces (e.g., ocean and dark vegetation), which was developed for the National Oceanic and Atmospheric Administration (NOAA) aboard the Advanced Very High-Resolution Radiometer (AVHRR) (Stow and Chen, 2002; Zhao et al., 2002) and Sea-star onboard Sea-viewing Wide-Field-of view Sensor (SeaWiFS) (Hsu et al., 2012; Sayer et al., 2012a; Sayer et al., 2012b). Being the Earth surface very complex because of its heterogeneity, variability, presence of anisotropic bidirectional characters, and high reflectance, the AOD retrieval is a great challenge. At present, with the new generation of satellite-onboard sensors, the AOD algorithms can be divided into five main categories: 1) Single-view spectral instrument methods; 2) Multiple view-angle spectral instrument methods (Kahn et al., 2009); 3) Polarization AOD algorithms; 4) AOD estimation from lidar instrument; and 5) AOD retrieval through a multi-sensor synergistic approach. More in detail, the single-view spectral instrument methods include contrast reduction methods, the Dark Target (DT) algorithm, the Deep Blue (DB) algorithm, the Multi-Angle Implementation of Atmospheric Correction (MAIAC) algorithm, the Simplified Aerosol Retrieval Algorithm (SARA), and the minimum Reflectance Technique (MRT). Among those techniques, Griggs (Griggs, 1975) used 0.55, 0.65, and $0.75\mu m$ wavelengths from ERTS/Landsat-1 aboard MSS (multispectral scanner) sensor and estimated AOD over ocean based on contrast reduction methods. Differently, Holben (Holben et al., 1992) used the Normalized Differential Vegetation Index (NDVI) and 3.75 μm wavelength from the NOAA aboard AVHRR sensor to retrieve the AOD over land based on the DT algorithms and contrast reduction methods. Based on the DT algorithm, Ouaidrari and Vermote (Ouaidrari and Vermote, 1999) also estimated AOD over land using red, blue, and green channels from the Landsat aboard TM sensor. Furthermore, the DT algorithm was applied to radiance data over land ($0.47\mu m$, $0.66\mu m$, $2.12\mu m$) and ocean ($0.87\mu m$) from Terra and Aqua aboard MODIS sensor to retrieve AOD (Remer et al., 2005; Levy et al., 2007a; Levy et al., 2007b). Instead, the DB algorithm uses the radiance data ($0.412\mu m$, $0.49\mu m$, and $0.67\mu m$) from MODIS and SeaWiFS sensors to estimate AOD over the bright reflecting surface (e.g., desert, arid and semi-arid surfaces (Hsu et al., 2004; Hsu et al., 2006)). The MAIAC algorithm uses blue ($0.47\mu m$), green ($0.550\mu m$), and NIR ($2.13\mu m$) MODIS bands to retrieve AOD over land (Lyapustin et al., 2011; Lyapustin et al., 2018). Bilal (Bilal et al., 2013; Bilal et al., 2014) developed the SARA algorithm, based on the MODIS sensor, which can estimate AOD at any wavelength over land. Finally, the MRT algorithm proposed by Wong (Wong et al., 2011) exploits reflectance observations (at $0.47\mu m$, $0.55\mu m$, $0.66\mu m$) from the MODIS sensor to retrieve the AOD over land. Furthermore, Grey (Grey et al., 2006) proposed the multi-view angle method to extract AOD over land using reflectance observations ($0.55\mu m$, $0.66\mu m$, $0.87\mu m$, $1.61\mu m$) from the AATSR instrument. Thomas (Thomas et al., 2009) developed a multi-view angle method named Global Retrieval of ATSR Cloud Parameters and Evaluation (GRAPE) method to estimate AOD at 550 nm over ocean and land using data from ATSR-2 and AATSR sensors. For retrievals over land and ocean, Diner (Diner et al., 1998; Diner et al., 2006; Diner et al., 2008) and Khan (Kahn et al., 2009) also used the multi-view angle method to extract AOD ($0.446\mu m$ and $0.558\mu m$). Deuze (Deuzé et al., 2001) and Tanrè (Tanré et al., 2011) developed the polarization method to estimate AOD over land and ocean using reflectance data ($0.49\mu m$, $0.67\mu m$, $0.865\mu m$) from POLDER sensor. The Selective Iterated Boundary Location (SIBYL) algorithm was developed to retrieve AOD from two channels at 532 nm and 1064 nm from the Cloud-Aerosol Lidar with Orthogonal Polarization (CALIOP) instrument onboard the Cloud-Aerosol Lidar and Infrared Pathfinder Satellite Observations (CALIPSO) satellite (Omar et al., 2013; Vaughn et al., 2009; Hu et al., 2009).

Satellite observations from the NASA Moderate Resolution Imaging Spectroradiometer (MODIS) MOD04 (0.55 μm) aerosol product (Levy et al., 2007b) and its higher resolution version Multi-Angle Implementation of Atmospheric Correction (MAIAC) (Chudnovsky et al., 2014) equally cannot provide AOD estimations at sub-kilometer resolutions. The dark target and deep blue MODIS NASA retrieval algorithms (Remer et al., 2005; Levy et al., 2007a), together with their simplified versions (Bilal et al., 2018), are still strongly dependent on complex radiative transfer look-up tables (LUT) or surface reflectance. In this paper, we describe the development of the High-rEsolution satellite image-based Aerosol optical Depth (HEAD) algorithm. This is an image-based estimation method that uses Kalman filters, similar to a predictive data compression (Bilal et al., 2018) applied to the high-resolution satellite imagery of urban environments to obtain AOD retrievals in the blue wavelength region at very high spatial resolution (up to 10 m). HEAD algorithm bridges two different spatial scales, permitting to study AOD variability at local and regional scales. HEAD retrieval algorithm does not need any prior assumption or radiative transfer look-up table (LUT) and it is independent on surface reflectance because in urban environment pixels in shadow are much easier to spot. The approach is assessed on four different test cases acquired by Landsat 8 involving two geographical areas in the United States and Thailand. A strong agreement with respect to the ground-based AERONET measurements is observed on several performance metrics.

The remaining of the paper is organized as follows. In Section 2, the data used to assess the algorithm performance are described, while Section 3 is devoted to the theory and assumptions behind the proposed HEAD approach. Furthermore, in Section 4, the extended Kalman filter for estimating the asymmetry factor is presented. Experimental results are shown in Section 5. Concluding remarks are drawn in Section 6.

2. Datasets

In this paper, we used the archived Landsat 8 (L8) OLI (Vermote et al., 2016) sensor multispectral images. To validate the algorithm, we follow an approach that prioritizes L8 images where multiple AERONET observations, considered as ground-truth, are available, instead of validating the algorithm at different sparse uncorrelated observational sites. This approach helps to better understand the importance of the spatial variability. For this reason, we acquired Landsat OLI images during the Distributed Regional Aerosol Gridded Observation (DRAGON) campaign that held in Boulder, Colorado (CO) metropolitan area in summer 2014. Moreover, to strength the validation process, the algorithm was also tested in Northern Thailand (Chiang-Mai metropolitan area), a region prone to biomass burning events during the monsoon season.

2.1. Satellite data

The multi-spectral Landsat 8 OLI (launched in February 2013) sensor bands have a spatial resolution of 30 m and a revisit time of 16 days. In this study, B1 (coastal) and B2 (blue) Landsat 8 OLI bands (Table 1) are considered to retrieve the AOD at 443 nm and 482 nm, respectively. The retrieved AOD is validated against the Version 3 (V3) Level 2 AERONET measured AOD in the same wavelength range.

2.2. AERONET aerosol optical depth

Following the approach in (Bilal et al., 2013), HEAD AOD retrievals are validated against AOD measurements taken by 16 AERONET temporary and permanent observational sites deployed in both rural and metropolitan areas around Boulder, CO during the 2014 Discovery-AQ campaign (Crawford and Pickering, 2014) and in a Southeast Asia region subject to massive biomass burning events during the monsoon season as in Chiang Mai, Thailand. The new Version 3 (V3) Level 2 AERONET data (Giles et al., 2019) are used for inter-comparison purposes. The AOD data show both high accuracy, with one standard deviation uncertainty of 0.02, and a positive bias of 0.02 (Giles et al., 2019). AERONET measurement data were obtained averaging the AOD values from 10 min prior to 10 min after satellite overpass. Table 2 shows the corresponding wavelength at which AERONET AOD is retrieved (column 2) to validate HEAD AODs from bands B1 (coastal) and B2 (blue), respectively. AERONET AOD values are corrected to match B1 and B2 wavelengths.

3. A dark target kalman filter algorithm for AOD estimation

The proposed retrieval algorithm estimates the AOD from the atmospheric path radiance, i.e., the scattered energy by the different constituents in the atmosphere that reaches the instrument telescope at the top-of-the-atmosphere without being reflected by the Earth's surface (Lolli et al., 2017). These techniques, which rely upon the path radiance estimation, have been widely used in image fusion, especially for pansharpening (Vivone et al., 2018a; Vivone et al., 2018b). In order to determine the path radiance and then the AOD, the original image is divided into patches with a statistically significant number of pixels. The common assumption in dark target based approaches for AOD retrieval is that the patch includes at least a dark target, i.e., a pixel having a surface reflectance equal to zero (practically, the dark target energy is only due to the atmosphere). This latter hypothesis seems hard to be verified in practice. Indeed, it is difficult to be find pure dark targets in nature (even for a limited wavelength range), thus invalidating the use of dark target based approaches for AOD estimation. For instance, it is worth to be remarked that vegetation and clear water show a reflectance ranging from 0.01 and 0.03 in the blue band (i.e., different from zero), thus representing “almost dark” targets for that band. Our approach deals with this crucial issue by relaxing the concept of dark target. In fact, the residual contribution of the surface reflectance can be considered as an additive noise filtering it out by using a Kalman filter, thus avoiding any interference in the final estimate. Hence, the proposed approach is independent from the surface reflectance and it is also able to take into account of the presence of the environment and/or instrumental noise. This is paid by the need of finding more than one “almost dark” object in the patch under

Table 1
Spectral bands, band numbers and central wavelengths [nm] of the L8 sensor.

Spectral band	Band number	Central wavelength
Coastal aerosol	B1	443.0
Blue	B2	482.0
Green	B3	561.5
Red	B4	645.5
Near infra-red	B5	865.0
Short-wave infra-red1	B6	1608.5
Short-wave infra-red2	B7	2200.5

Table 2
Spectral bands and central wavelengths [nm] of the L8 data (left column) used in this study and the corresponding AERONET AOD wavelength (right column).

L8 OLI	AERONET
B1[443.0]	440
B2[482.0]	500

analysis.

The optical image consists of spectral reflectances, $\rho_T(\lambda,\theta_s,\theta_v,\phi)$, where λ is the considered wavelength, θ_s the solar zenith angle, θ_v the view zenith angle, and ϕ the relative zenith angle. From the top-of-the-atmosphere (TOA) radiance, $L_T(\lambda,\theta_s,\theta_v,\phi)$, ρ_T can be calculated as follows (Bilal et al., 2013):

$$\rho_T(\lambda,\theta_s,\theta_v,\phi)=\frac{\pi d^2 L_T(\lambda,\theta_s,\theta_v,\phi)}{E^0(\lambda)cos(\theta_s)}, \tag{1}$$

where d is the Sun-Earth distance in astronomical units and $E^0(\lambda)$ is the solar spectral irradiance.

ρ_T is defined as the sum of three terms (Bilal et al., 2013):

$$\begin{aligned}\rho_T(\lambda,\theta_s,\theta_v,\phi)=&\rho_A(\lambda,\theta_s,\theta_v,\phi)+\rho_R(\lambda,\theta_s,\theta_v,\phi)\\&+f(\rho_S(\lambda,\theta_s,\theta_v,\phi)),\end{aligned} \tag{2}$$

where ρ_A is the TOA reflectance term accounting for aerosol scattering, ρ_R is the term accounting for molecular scattering (Rayleigh), and $f(\cdot)$ is a function of the surface reflectance, ρ_S, with $f(x)>0$ if $x>0$ and $f(0)=0$.

The first goal is to isolate the contribution due to ρ_A in (2). On one hand, ρ_R could be easily calculated and compensated in (2) (Bilal et al., 2019) using ancillary data. On other hand, no analytical expression exists for ρ_S. Thus, after estimating and then compensating ρ_R (Bilal et al., 2019), we assume the presence of a dark object in the scene, i.e., an object that has $\rho_S(\lambda,\theta_s,\theta_v,\phi)=0$, thus having $f(\rho_S(\lambda,\theta_s,\theta_v,\phi))=0$.

Once identified, the dark object TOA reflectance is only due to ρ_A.[1] Thus, the AOD $\tau_A(\lambda)$ can be calculated starting from ρ_A as follows:

$$\tau_A(\lambda)=\frac{4cos(\theta_s)cos(\theta_v)}{\omega_0 P_a(\theta_s,\theta_v,\phi)}\rho_A(\lambda,\theta_s,\theta_v,\phi), \tag{3}$$

where ω_0 is the single-scattering albedo term, which accounts for aerosol absorption ($\omega_0=1$ indicates full scattering aerosols, $\omega_0=0$ denotes full absorbing aerosols), P_a is the approximated phase function as defined in (Henyey and Greenstein, 1941).

$$P_a(\theta_s,\theta_v,\phi)=\frac{1-[g(\lambda)]^2}{\left\{1+[g(\lambda)]^2-2g(\lambda)cos(\Theta)\right\}^{3/2}}, \tag{4}$$

Θ is the scattering angle (if the sensor and sun are exactly at nadir, the angle is π), and $g(\lambda)$ is the asymmetry factor that reflects the wavelength dependent particle scattering energy angular distribution ($g(\lambda)=1$ indicates forward scattering, $g(\lambda)=0$ denotes homogeneous scattering and $g(\lambda)=-1$ indicates backscattering).

The following assumptions are required in order to retrieve the acquired scenario AOD: *i*) at least a dark object is acquired, *ii*) the aerosol loading can be considered homogeneous over the considered patch, *iii*) the contribution due to the Rayleigh scattering is properly compensated from the total TOA reflectance, ρ_T, and *iv*) the absence of any kind of noise in the TOA reflectance measurements. If all these hypotheses are valid, the dark object can be simply found getting the minimum value of ρ_T for all the acquired TOA reflectances in a given image patch (a subset with a proper size of the whole image). This is because $f(x)>0$ if $x>0$ and $f(0)=0$ and, hence, a value of $\rho_S>0$ can only increase the value of ρ_T. This method will be called *Minimum* from hereon. By analyzing the four hypotheses, the third assumption is reasonable. Instead the second assumption can be only locally valid, especially if the acquired scene contains aerosol emission sources (i.e., the aerosol load should be considered homogeneous into the patch of a given size). Thus, the selection of the block size is crucial. Indeed, the existing trade-off between the first and the second assumptions is straightforward: the greater the block, the higher the probability to find a dark object, but the second assumption could be not valid. Instead, the smaller the block, the higher the probability to get the second assumption verified, but the first assumption could be not valid.

It is worth to be remarked that the first and fourth assumptions are hardly verified in practice having a clear impact on the performance in estimating τ_A. Thus, in order to consider noisy images with a residual contribution of $\rho_S(\lambda,\theta_s,\theta_v,\phi)$ in (2) due to the consideration of "almost dark" targets, a sequential Bayesian filtering problem is proposed. In particular, we can relax the first assumption, i.e., assuming that more than one "almost dark" object is present (e.g., the p-th percentile of the distribution of the TOA

[1] Remember that ρ_R can easily be compensated using the formula in (Bilal et al., 2019).

reflectances is due to "almost dark" objects). It is worth to be noted that "almost dark" objects are easy to find because there are many examples of natural structures that have the same behavior of "almost dark" objects, but only for a limited wavelength range, e.g., large water bodies in the near-infrared spectrum or vegetation in the red band. It is even more easier to spot them in the blue wavelength range because, in the visible spectrum, the atmospheric transmittance is lower at shorter wavelengths with respect to the higher ones. Moreover, thanks to the use of the proposed Bayesian approach, we can remove the fourth hypothesis (the noise is indeed filtered out by the Kalman filter). Thus, the "almost dark" object TOA reflectances can be seen as observations in a Bayesian filter, say $\{z_k\}_1^K$, where K is the number of the "almost dark" objects in the acquired scene. The state after k observations, say x_k, is represented by the AOD, $\tau_A(\lambda)$. The dynamic model is defined as follows:

$$x_k = x_{k-1} + w_k, \tag{5}$$

where $w_k \sim \mathcal{N}\left(0, \sigma_w^2\right)$ is the process noise that can be modeled as a Gaussian with zero-mean and variance ${\sigma_w}^2$. The observations $\{z_k\}_1^K$ are related to the state to be estimated, x_k, through the following observation model:

$$z_k = Hx_k + n_k, \tag{6}$$

where, following (3), H is set as

$$H = \frac{\omega_0 P_a(\theta_s, \theta_v, \phi)}{4cos(\theta_s)cos(\theta_v)} \tag{7}$$

and $n_k \sim \mathcal{N}\left(0, \sigma_n^2\right)$ is the measurement noise that is modeled as a Gaussian with zero-mean and variance ${\sigma_n}^2$ accounting for instrumental noise, uncompensated molecular scattering, and residual surface contributions due to the use of not pure dark objects.

Considering the linearity of the dynamic and observation models and that both the process noise and measurement noise are white, the optimal filter (in the sense of minimum mean squared error) is the Kalman filter (Bar-Shalom and Li, 1995). Hence, the estimation of the AOD at step k (after k observations), i.e., $\widehat{x}_{k|k}$, can be obtained starting from an initial value, $\widehat{x}_{0|0}$, and the related error covariance matrix, P_k, say $P_{0|0}$, exploiting the following equations (Bar-Shalom and Li, 1995):

1. Prediction step.

$$\widehat{x}_{k|k-1} = \widehat{x}_{k-1|k-1}, \tag{8}$$

$$P_{k|k-1} = P_{k-1|k-1} + \sigma_w^2. \tag{9}$$

2. Update step.

$$\widehat{x}_{k|k} = \widehat{x}_{k|k-1} + K_k\left(z_k - H\widehat{x}_{k|k-1}\right), \tag{10}$$

$$P_{k|k} = P_{k|k-1} - K_k S_k K_k^T, \tag{11}$$

where

$$K_k = P_{k|k-1}H^T S_k^{-1} \tag{12}$$

is the Kalman gain, $\cdot^T$ is the transpose operator and

$$S_k = HP_{k|k-1}H^T + \sigma_n^2. \tag{13}$$

The final estimate of the AOD, $\tau_A(\lambda)$, is $\widehat{x}_{K|K}$, namely the state obtained after presenting to the Kalman filter all the K observations (i.e., the "almost dark" objects in a given patch under analysis).

4. An extended Kalman filter for asymmetry factor estimation

This section is devoted to the presentation of the proposed extended Kalman filter (Bar-Shalom and Li, 1995) for the estimation of the asymmetry factor. Again, the reflectances provided by the "almost dark" objects, denoted as $\{z_k\}_1^K$, become the observations of the Bayesian filter. Instead, for this problem, the state to be estimated, x_k, is the previously defined asymmetry factor $g(\lambda)$. Again, the dynamic model followed by $g(\lambda)$ is the same as the one used to estimate $\tau_A(\lambda)$, i.e.,

$$x_k = x_{k-1} + w_k, \tag{14}$$

where $w_k \sim \mathcal{N}\left(0, \sigma_{g,w}^2\right)$ is the process noise that can be modeled as a zero-mean Gaussian distribution with variance ${\sigma_{g,\,w}}^2$. The observations $\{z_k\}_1^K$ are related to the state to be estimated, x_k, through the following non-linear observation model:

$$z_k = h(x_k) + n_k, \tag{15}$$

where, from (3), (4) and considering $x_k = g(\lambda)$,

$$h(x_k) = \frac{\omega_0}{4cos(\theta_s)cos(\theta_v)} \frac{1 - x_k^2}{[1 + x_k^2 - 2x_k cos(\Theta)]^{3/2}} \tau_A(\lambda) \tag{16}$$

and $n_k \sim \mathcal{N}\left(0, \sigma_{g,n}^2\right)$ is the measurement noise that can be modeled as a zero-mean Gaussian distribution with variance ${\sigma_{g,n}}^2$ accounting for instrumental noise, uncompensated molecular scattering, and residual surface contributions due to the use of not pure dark objects. It is worth to be noted that in this case $\tau_A(\lambda)$ represents an input of the $g(\lambda)$ estimation procedure.

Considering that the observation model is non-linear, an Extended Kalman Filter (EKF), which is linearized about an estimate of the current mean and covariance, is exploited (Bar-Shalom and Li, 1995). In particular, the state observation matrix is defined to be the following Jacobian, i.e.,

$$H_k = \left.\frac{\partial h}{\partial x_k}\right|_{\widehat{x}_{k|k-1}}, \tag{17}$$

where $\widehat{x}_{k|k-1}$ is the state prediction at step k defined as for τ_A. The matrix H_k is calculated according to (17) and, considering the non-linear model in (16), we have

$$H_k = \frac{w_0}{4\mu_v \mu_s hc_k^3} \tau_A(\lambda) hf_k, \tag{18}$$

where

$$hf_k = -2\widehat{x}_{k|k-1} hc_k^{3/2} - 3\left(1 - \widehat{x}_{k|k-1}^2\right) hc_k^{0.5} [\widehat{x}_{k|k-1} + cos(\Theta)] \tag{19}$$

and

$$hc_k = 1 + \widehat{x}_{k|k-1}^2 - 2\widehat{x}_{k|k-1} cos(\Theta). \tag{20}$$

The same Kalman filter prediction equations for $\widehat{x}_{k|k-1}$ and $P_{k|k-1}$ in (8) and (9) are exploited in this case. Instead, starting from the linearization of $h(\cdot)$, H_k in (18), the state update equation becomes (Bar-Shalom and Li, 1995):

$$\widehat{x}_{k|k} = \widehat{x}_{k|k-1} + K_k[z_k - h(\widehat{x}_{k|k-1})] \tag{21}$$

where

$$K_k = P_{k|k-1} H_k^T \left(H_k P_{k|k-1} H_k^T + \sigma_{g,n}^2\right)^{-1}. \tag{22}$$

Instead, the covariance matrix update equation is given by

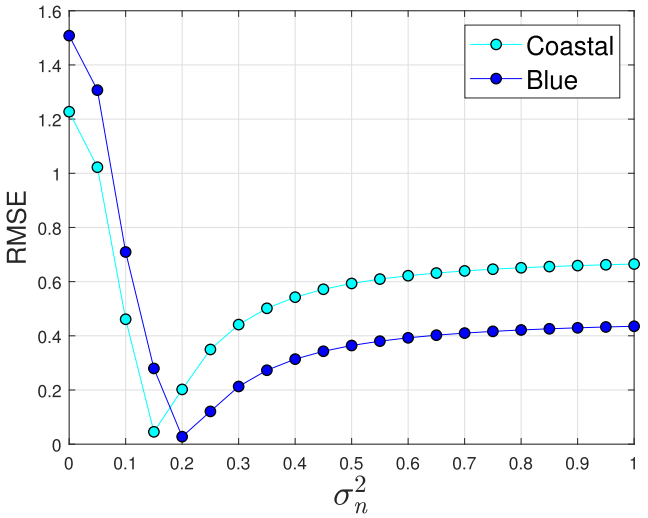

Fig. 1. Multi-variate analysis to optimize the ${\sigma_n}^2$ parameter for the Chiang Mai dataset acquired on 20 March 2014. The value is independent on the scenario under analysis.

$$P_{k|k} = [1 - K_k H_k] P_{k|k-1}. \tag{23}$$

Again, the final estimate of the asymmetry factor, $g(\lambda)$, is represented by $\widehat{x}_{K|K}$, namely, the state after presenting all the K observations to the EKF.

5. Experimental results

This section is devoted to the presentation of the experimental results about the estimation of the AOD and the related performance assessment. Furthermore, an example about the estimation of the asymmetry factor is also provided.

As described in Sections 3 and 4, the Kalman filter should be optimized with respect to the parameters that take into consideration both the observational and instrumental noises. In particular, the ${\sigma_n}^2$ parameter plays a role of crucial importance representing the additive noise in the observation model in (6). After carried out a multivariate analysis on different LANDSAT 8 OLI images, the results put in evidence that its optimal value is around 0.2. An instance of the optimization process is shown in Fig. 1 for the Chiang Mai dataset acquired on 20 March 2014. In particular, the root mean square error metric between the estimated values from the Kalman filter and the AERONET observations (ground-truth) is minimized. The minimum for both the spectral bands is around 0.2 justifying this choice. For the other parameters describing the aerosol microphysical properties as $g(\lambda)$ and $\omega_0(\lambda)$, required in order to use the model in (3) and (4), the setting is less crucial. The retrieval is much more sensitive to the asymmetry factor $g(\lambda)$ than the single scattering albedo $\omega_0(\lambda)$. We arbitrarily fix the values of $\omega_0(\lambda)$ and $g(\lambda)$ to make HEAD algorithm independent of the aerosol type. The values were chosen accordingly with AERONET climatological data. We are aware that this choice can introduce errors especially in some particular cases, e.g., pure dust or ash outbreaks. However, as shown in the next section, this choice is corroborated by the excellent agreement obtained between HEAD retrievals and AERONET observation data in two very different regions of the world as Colorado and Thailand. Thus, default values for $\omega_0(\lambda)$ and $g(\lambda)$ are exploited in the AOD estimation test cases and reported in Table 3, which is related to the Chiang Mai test case in Fig. 1. It is worth to be pointed out that Table 3 also shows the values of some angles that are about the particular acquisition geometry. The setting of these parameters is easy because they can be obtained by accessing to the meta data of the particular Landsat 8 acquisition.

HEAD performance is assessed together with its effectiveness, against the ground-based AERONET observations, in two locations, i.e., Colorado (USA) and Thailand. As suggested in (She et al., 2019), the AERONET data are inter-compared with an averaged value of HEAD over a patch of $300m \times 300m$ image window.

In the next paragraphs, we present the HEAD retrievals on four images, two obtained in Colorado and two in Northern Thailand. For each case, we reported the geo-referenced images of the LANDSAT 8 OLI TOA reflectances for band B1 and B2, respectively, together with the names of the AERONET observational stations. Afterwards, HEAD retrievals are reported for each band for the Minimum method, used as baseline, and the proposed Kalman filter approach exploiting the parameters as in Table 3.

5.1. 02 July 2014, Colorado, USA

In this first case study, the AOD retrieved from HEAD for coastal (B1) and blue (B2) bands is showed. The proposed scenario is the region around Boulder, CO, during the NASA Discover-AQ campaign. The main study area extends along the Northern Front Range from the Denver metropolitan area in the south to Fort Collins in the north extending eastward from the mountains as far as Greeley. This area contains a diverse mixture of air pollution sources that include transportation, power generation, oil and gas extraction, agriculture, natural vegetation and episodic wildfires. The region being studied often experiences ozone levels in summer that exceed national US health standards. Ground-level ozone is chemically produced from the combination of nitrogen oxides and hydrocarbon emissions in sunlight. The Colorado study is the final stop in a series of four field studies by the DISCOVER-AQ team focused on areas across the United States that routinely experience poor air quality. As shown in Fig. 2, in the analyzed image, nine AERONET stations are present. Few scattered clouds are contaminating the image and they are visible in the lower left corner. Fig. 3 shows the AOD estimations of the compared approach for the two analyzed spectral bands. In Table 4, the different AERONET stations show rather homogeneous values over the region under analysis with AOD values ranging in the interval 0.27–0.36 for band B2. Chatfield Pk (South-East) is the station recording the lower AOD while Boulder is recording the higher values. HEAD algorithm exploiting Kalman

Table 3
Values used to retrieve the AOD in Fig. 1 for B1 (coastal) and B2 (blue) bands, respectively, for the Chiang Mai dataset acquired on 20 March 2014.

Parameter	Value
θ_s	24.76°
θ_v	0°
Θ	155.24°
${\sigma_n}^2$	0.2
${\sigma_w}^2$	0.1
λ	0.44–0.48 μm
$g(\lambda)$	0.55 (for both B1 and B2)
$\omega_0(\lambda)$	0.915 (for both B1 and B2)

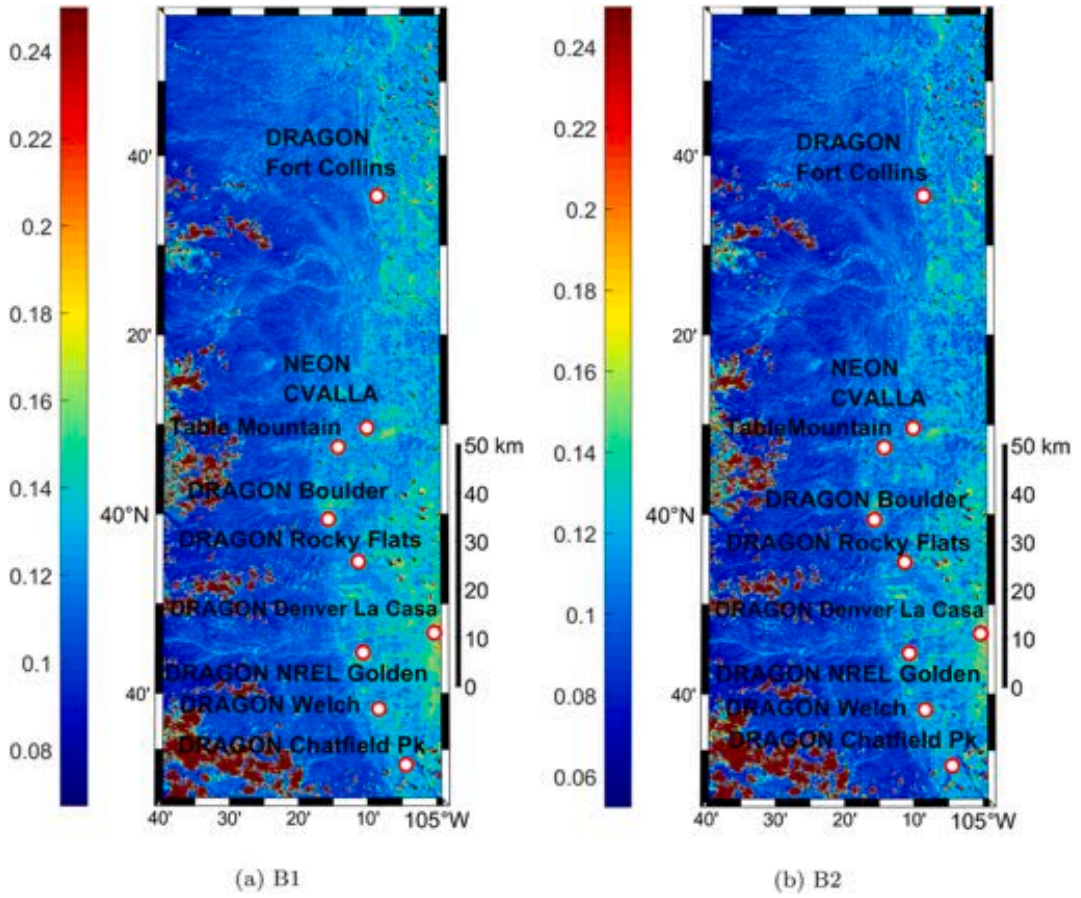

Fig. 2. LANDSAT OLI 8 TOA reflectance on 02 July 2014 during the AERONET DRAGON campaign. The names of the AERONET stations used during the validation process are also reported. Cloud contamination is visible especially in the left lower corner.

filtering is on general underestimating the AERONET values, but still the agreement is very good and much better than using the Minimum approach. Fig. 2 shows how much the minimum method is under-evaluating the AOD.

5.2. 12 August 2014, Colorado, USA

The second proposed case study is taken again during the NASA Discover-AQ campaign in Bouder region, Colorado. In this day, five AERONET stations are available for performance assessment, see Fig. 4. The atmosphere is cleaner with respect to 02 July 2014. The five stations show an AOD ranging from 0.11 to 0.17 for coastal band and 0.09–0.13 for blue band, see Table 5. Boulder is again the station showing the higher values while Welch, on the Southwest, the lower values. The proposed HEAD approach shows a much better agreement with AERONET observations with respect to the Minimum. On average, over the five stations, HEAD has a difference of 0.03 for B1 and 0.01 for B2, while for the Minimum it is 0.1 and 0.06, respectively. In Fig. 5, patterns are clearly visible in the AOD with higher values in the North, clearer zones in the center, and peaks in the Southwest, compatible with local air pollution linked to some metropolitan areas.

5.3. 20 March 2014, Chiang Mai, Thailand

The considered LANDSAT 8 OLI image shows the Northern Thailand region, centered in the metropolitan area of Chiang Mai on 20 March 2014, see Fig. 6. Chiang Mai is surrounded by forest and agricultural fields. The air pollution occurs in the dry season every year and biomass burning has been known as a major source. In March, intense episodes of biomass burning events are reported. A smoke creek is clearly visible in the center of the image (Fig. 7). The region is also affected by pollution related to urban activities, e.g., road traffic and domestic cooking. The area is not part of any DRAGON campaign, for this reason, only an AERONET station is available. At glance in Fig. 7, it is clearly visible a smoke creek (red areas) over the Chiang Mai metropolitan area. The red features highlight intense biomass burning aerosol presence, with very high values reaching peaks of 2.5 for the AOD, while the Northeast part is showing a much clearer atmosphere of about 0.6. The inter-comparison in Table 6 with the single AERONET station, again, put in evidence how the HEAD Kalman filter performance is much better with respect to the Minimum, with an error of about 10% against 50%.

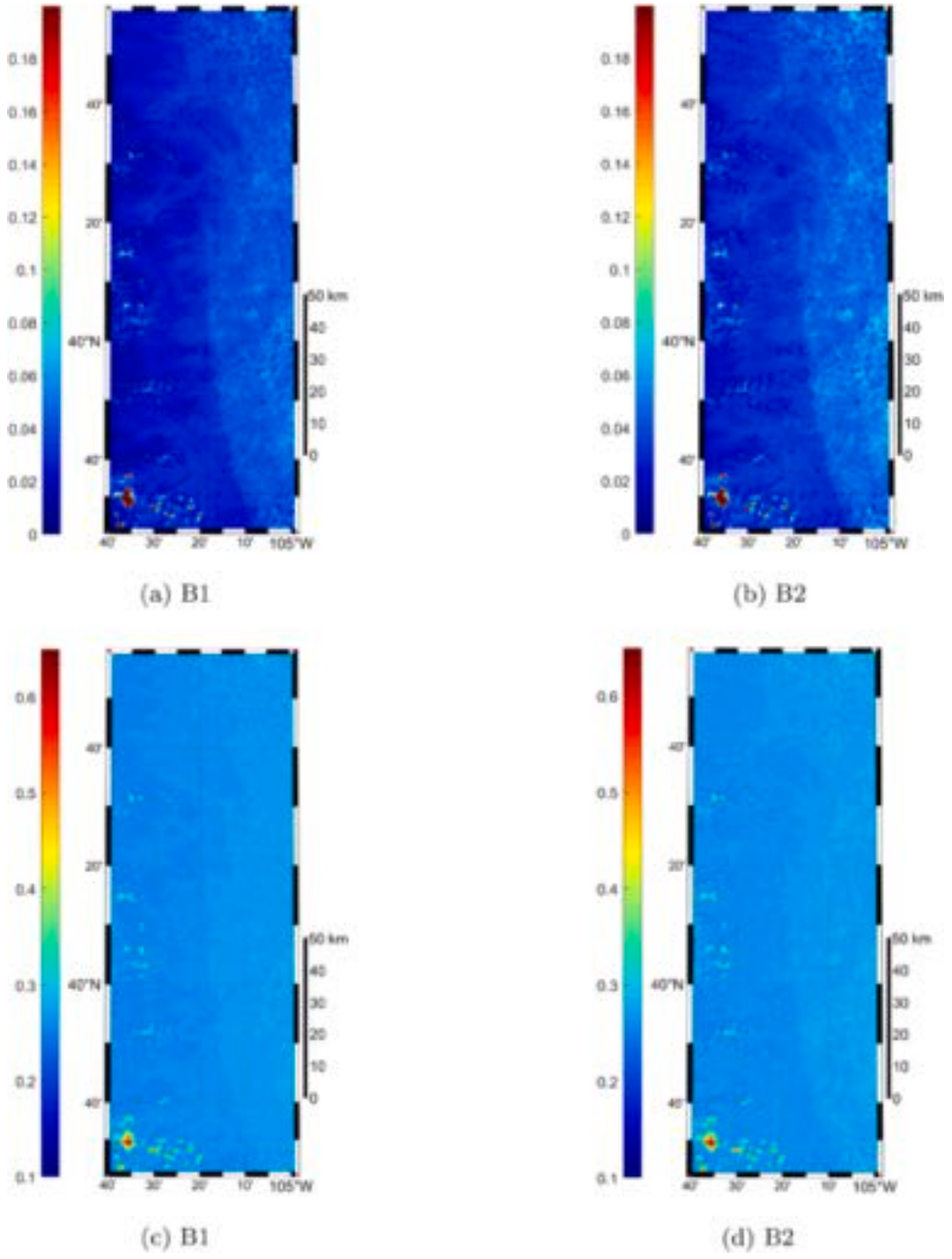

Fig. 3. AOD retrieved from LANDSAT 8 OLI reflectance (Fig. 2) with the Minimum (a) and (b) and the Kalman filter (c) and (d) on 02 July 2014 in Colorado during the NASA DISCOVERY-AQ campaign.

5.4. 09 March 2016, Chiang Mai, Thailand

The last considered LANDSAT 8 OLI image represents another biomass burning episode in Chiang Mai region on 09 March 2016, as shown Fig. 8. In this case, the aerosol loading is lower with respect to 20 March 2014, but several aerosol sources are present in the region. In the Southwest, aerosol layers reaching very high values of AOD, up to 2, are present, as shown in Fig. 9. In the center of the figure, instead, a region with cleaner air is clearly visible. Again, Table 7 reports how much HEAD is closer to the AERONET

Table 4
Colorado dataset (date: 02 July 2014). δ_{B1} and δ_{B2} are the absolute errors between the estimated AOD and the reference AERONET observations. Best results are in boldface.

	AERONET		KF				Minimum			
	B1	B2	B1	B2	δ_{B1}	δ_{B2}	B1	B2	δ_{B1}	δ_{B2}
DRAGON Boulder	0.357	0.301	0.268	0.280	**0.090**	**0.021**	0.314	0.252	0.043	0.049
DRAGON Chatfield Pk	0.269	0.227	0.262	0.265	**0.006**	**0.039**	0.036	0.041	0.232	0.185
DRAGON Denver La Casa	0.340	0.285	0.275	0.280	**0.065**	**0.005**	0.050	0.056	0.289	0.229
DRAGON Fort Collins	0.309	0.258	0.274	0.278	**0.035**	**0.020**	0.041	0.046	0.268	0.212
DRAGON NREL Golden	0.315	0.265	0.269	0.273	**0.047**	**0.008**	0.045	0.051	0.270	0.214
DRAGON Rocky Flats	0.292	0.245	0.267	0.272	**0.025**	**0.027**	0.042	0.048	0.250	0.197
DRAGON Welch	0.302	0.252	0.275	0.270	**0.032**	**0.023**	0.045	0.053	0.256	0.199
NEON CVALLA	0.333	0.283	0.267	0.271	**0.066**	**0.012**	0.044	0.049	0.289	0.233
Table Mountain	0.332	0.280	0.267	0.272	**0.065**	**0.008**	0.043	0.050	0.289	0.230

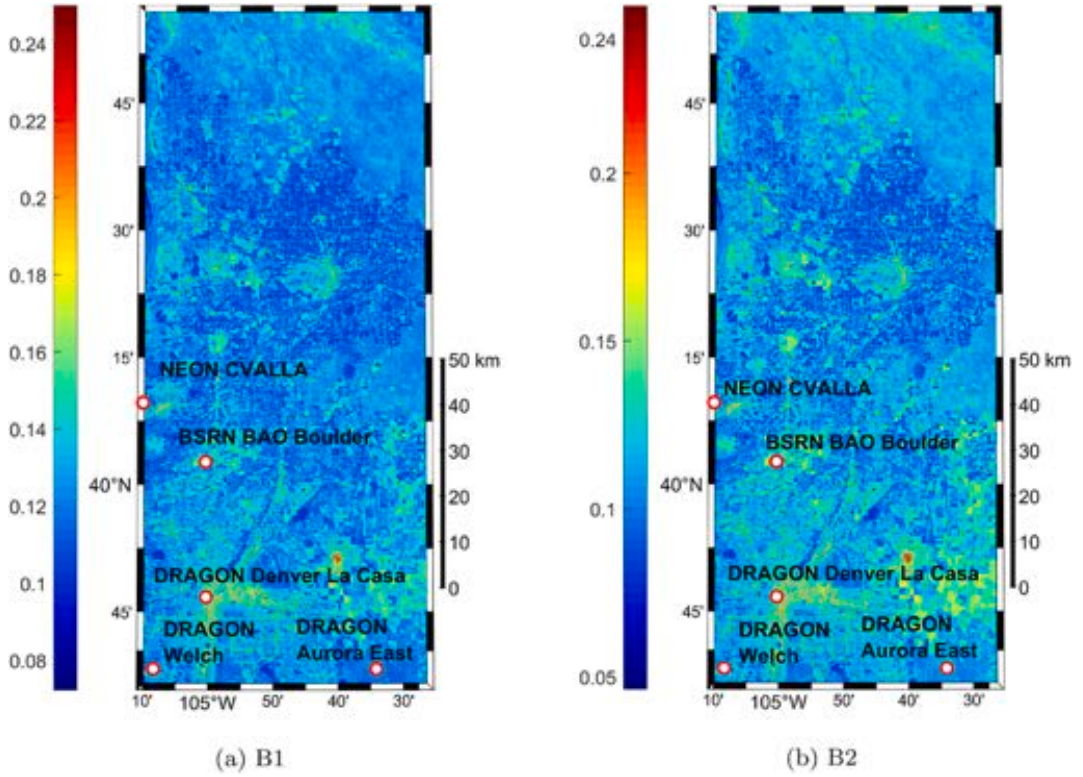

Fig. 4. LANDSAT OLI 8 TOA reflectance on 12 August 2014 during the AERONET DRAGON campaign. The names of the AERONET stations used during the validation process are also reported.

Table 5
Colorado dataset (date: 12 August 2014). δ_{B1} and δ_{B2} are the absolute errors between the estimated AOD and the reference AERONET observations. Best results are in boldface.

	AERONET		KF				Minimum			
	B1	B2	B1	B2	δ_{B1}	δ_{B2}	B1	B2	δ_{B1}	δ_{B2}
BSRN BAO Boulder	0.167	0.136	0.121	0.132	**0.047**	**0.003**	0.055	0.069	0.112	0.067
DRAGON Aurora East	0.148	0.120	0.113	0.124	**0.035**	**0.005**	0.045	0.056	0.102	0.064
DRAGON Denver La Casa	0.154	0.122	0.117	0.123	**0.037**	**0.001**	0.047	0.052	0.107	0.070
DRAGON Welch	0.116	0.094	0.112	0.119	**0.004**	**0.025**	0.043	0.051	0.073	0.043
NEON CVALLA	0.151	0.128	0.116	0.118	**0.034**	**0.010**	0.047	0.054	0.103	0.074

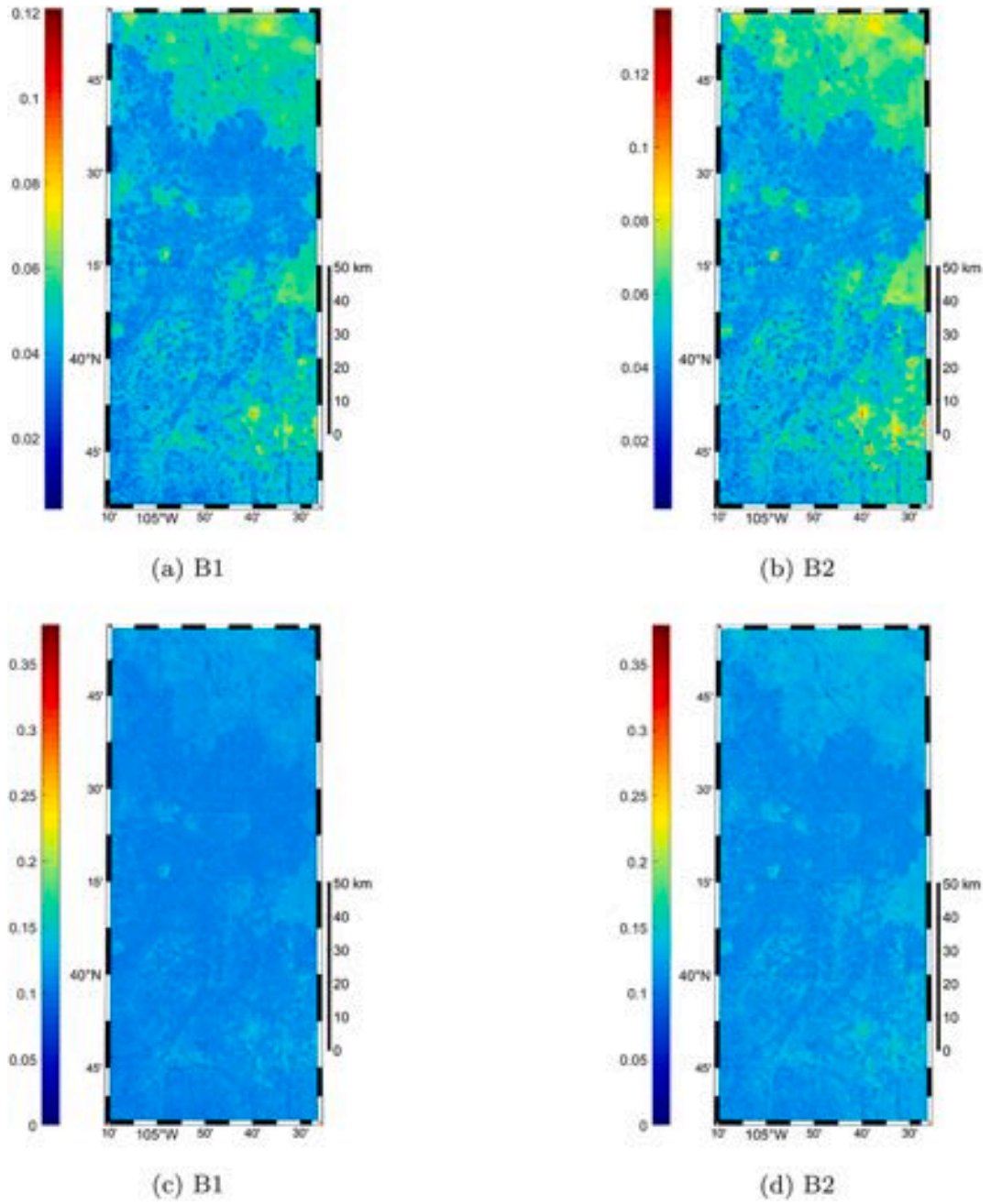

Fig. 5. AOD retrieved from LANDSAT 8 OLI reflectance (Fig. 4) with the Minimum (a) and (b) and the Kalman filter (c) and (d) on 12 August 2014 in Colorado during the NASA DISCOVERY-AQ campaign.

observation taken as reference, with an improvement of 40% with respect to the Minimum.

5.5. *Overall performance using AERONET ground-based stations*

For the case studies analyzed in the previous sections, we report in Table 8 the overall performance of the HEAD algorithm with respect to AERONET observations considered as reference. We used three different metrics for evaluation. The first index is the Root Mean Square Error (RMSE) in (24), which assumes that the differences between the satellite retrieval method and ground-based observations are normally distributed (Lolli et al., 2013).

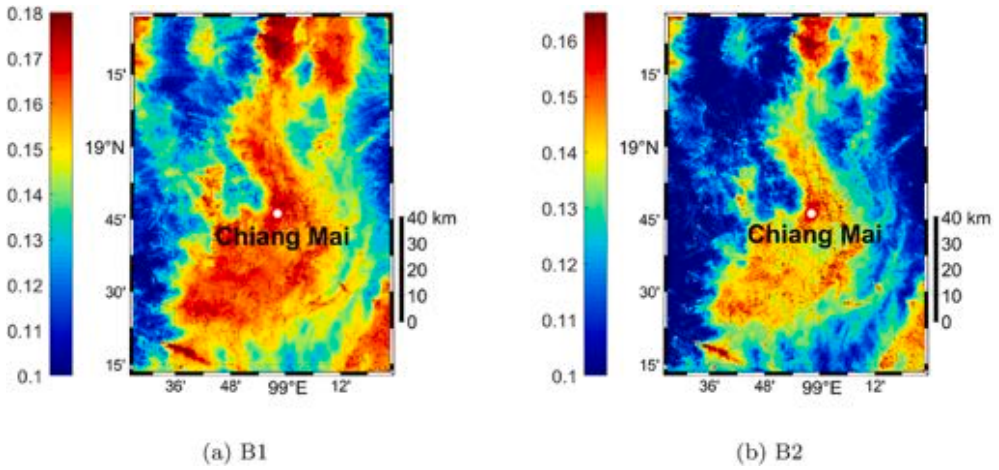

Fig. 6. LANDSAT OLI 8 TOA reflectance on 20 March 2014 in Chiang Mai, Thailand, during an intense biomass burning event.

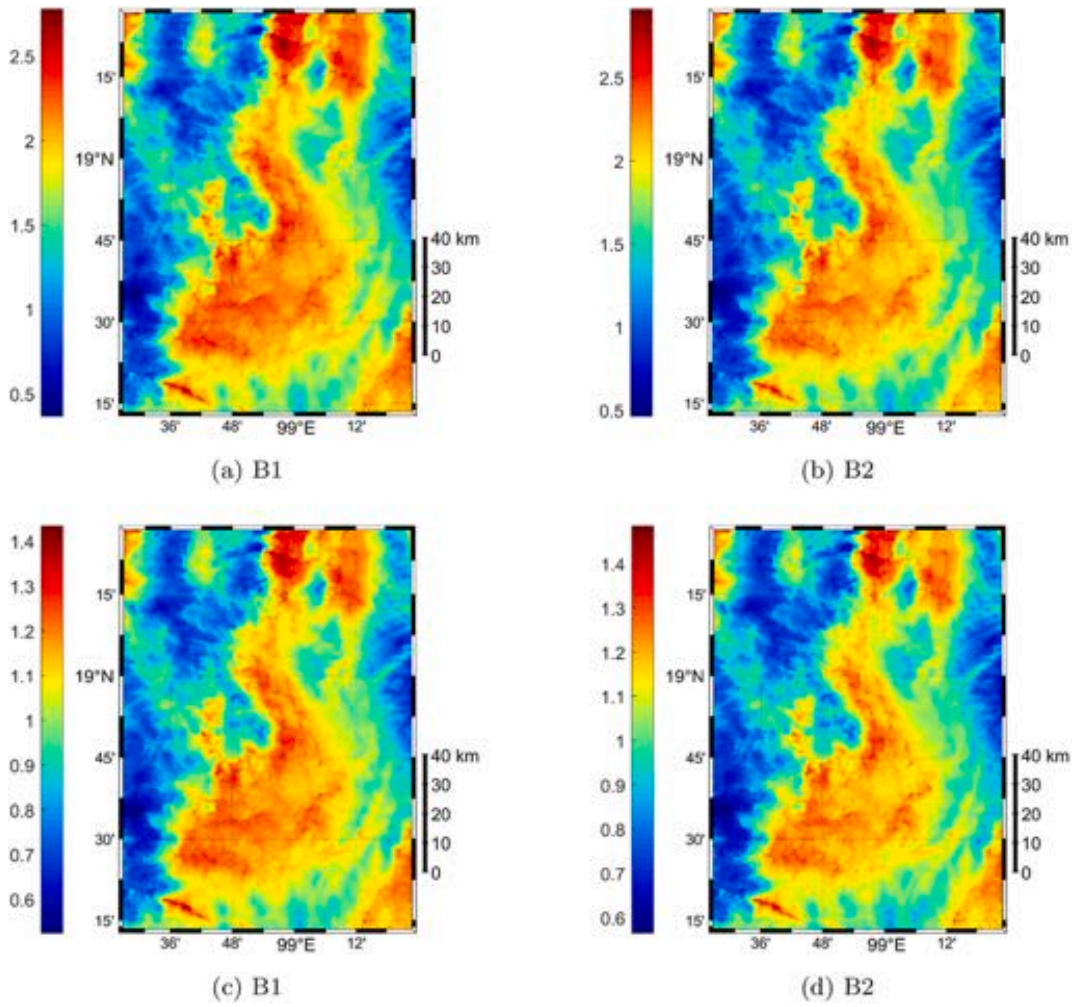

Fig. 7. AOD retrieved from LANDSAT 8 OLI reflectance (Fig. 6) with the Minimum (a) and (b) and the Kalman filter (c) and (d) on 20 March 2014 in Chiang Mai, Northern Thailand, during an intense biomass burning event.

Table 6
Chiang Mai dataset (date: 20 March 2014). δ_{B1} and δ_{B2} are the absolute errors between the estimated AOD and the reference AERONET observations. Best results are in boldface.

	AERONET		KF				Minimum			
	B1	B2	B1	B2	δ_{B1}	δ_{B2}	B1	B2	δ_{B1}	δ_{B2}
Chiang Mai	1.290	1.060	1.214	1.263	**0.076**	**0.203**	2.311	2.382	1.021	1.322

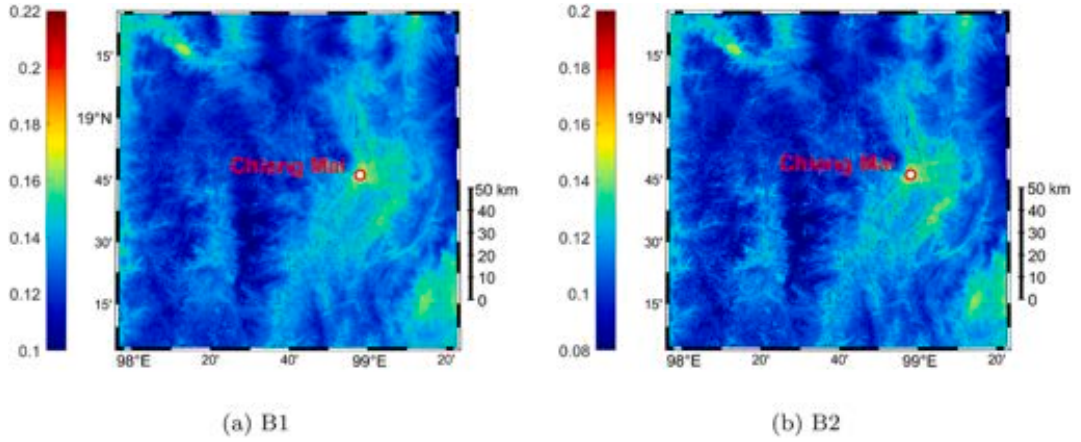

Fig. 8. LANDSAT OLI 8 TOA reflectance on 09 March 2016 in Chiang Mai, Thailand, during an intense biomass burning event.

$$\mathrm{RMSE} = \sqrt{\frac{\sum_{i=1}^{n} (AODaero_i - AODsat_i)^2}{n}}, \tag{24}$$

where the RMSE is the average deviation between the i-th AERONET AOD ($AODaero_i$) and the satellite retrieved AOD ($AODsat_i$) for the pixel containing the AERONET station, with n the total measurement number. The ideal RMSE value is zero.

The second index is the Mean Absolute Error (MAE) in (25). The difference with respect to the RMSE is that the MAE is less sensitive to large errors. The RMSE is always greater or equal to MAE.

$$\mathrm{MAE} = \frac{1}{n} \sum_{i=1}^{n} | AODaero_i - AODsat_i | . \tag{25}$$

The ideal MAE value is zero. The last metric is the Root Mean Bias (RMB) in (26):

$$\mathrm{RMB} = \frac{\overline{AODsat}}{\overline{AODaero}}, \tag{26}$$

where $\bar{\cdot}$ is the average operator.

If the RMB values are <1, we are in presence of underestimation, while the opposite is true for values >1. The ideal value is 1.

The outcomes in Table 8 are obtained averaging the results over B1 and B2 bands. Both for Kalman filter and the Minimum, the RMSE and the MAE highlight that error variance is very small. From the RMB, instead, it can be noticed that the Minimum is strongly underestimating the AOD AERONET values in Colorado, USA, while is strongly overestimating the ground-based observations in Thailand, whereas Kalman filter RMB values are close to 1 for both the scenarios indicating that the HEAD approach strongly improves the AOD retrieval based on the Minimum.

Finally, Fig. 10 depicts a comprehensive validation using all the AERONET observations for all the images. Overall, the HEAD (black dots, black line) shows a very good agreement with the ground-based observation for both coastal and blue bands. The green and the black optimal lines are very close and almost superimposed, while the red line, representing the Minimum, shows substantial differences. (See Fig. 11.)

6. Concluding remarks

Aerosol emissions play a fundamental role in modulating incoming solar radiation (direct effects), in acting as ice-nuclei for cloud formation (indirect effects) and in changing the thermodynamic properties of the atmospheric column (semi-direct effects). Moreover, natural and anthropogenic aerosol advections over large metropolitan areas can exacerbate air-pollution and promote haze formation, a threat for transports and population. For these reasons, monitoring the aerosol loading is of fundamental importance, especially in

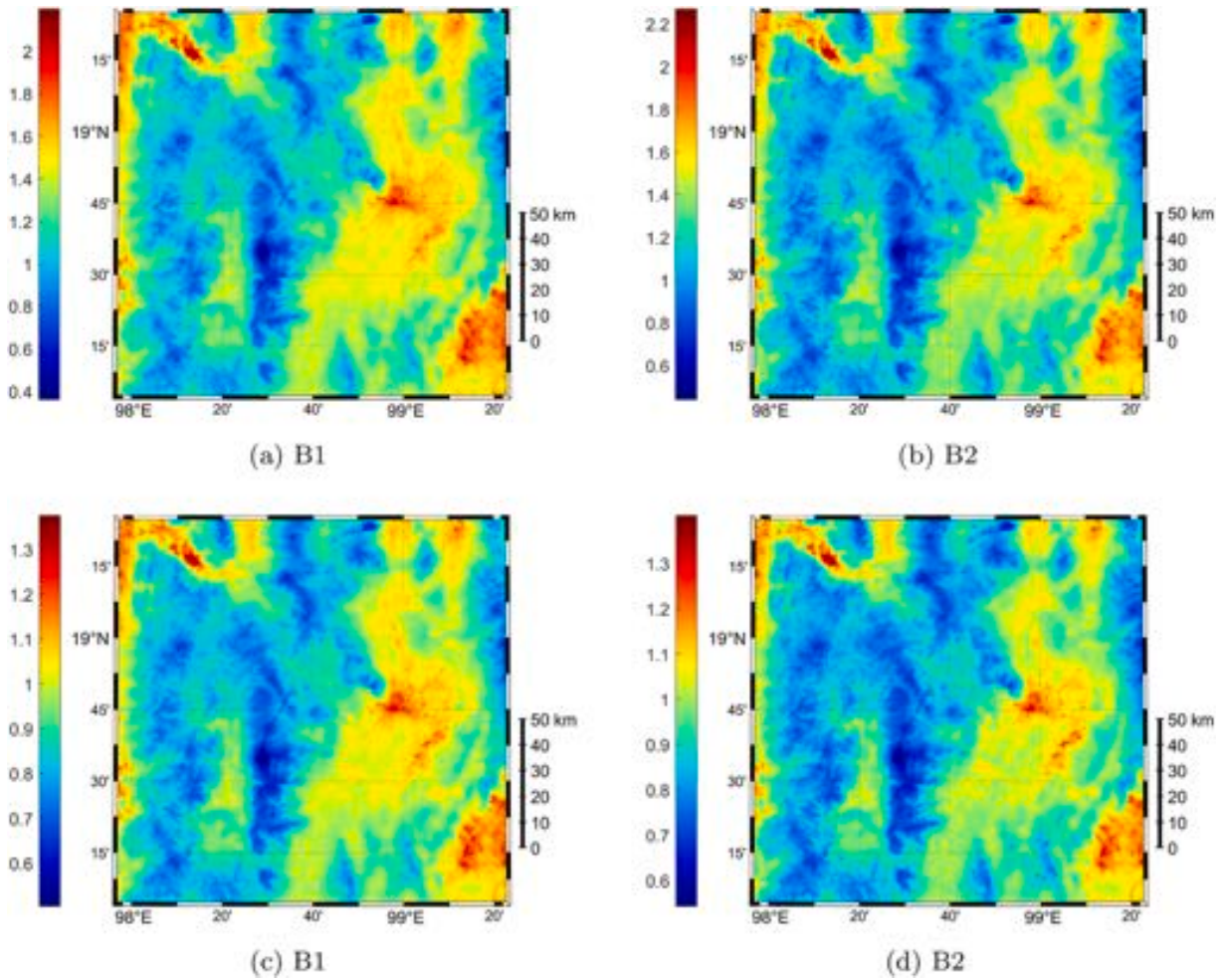

Fig. 9. AOD retrieved from LANDSAT 8 OLI reflectance (Fig. 8) with the Minimum (a) and (b) and the Kalman filter (c) and (d) on 09 March 2016 in Chiang Mai, Northern Thailand, during an intense biomass burning event.

Table 7
Thai dataset (date: 09 March 2016). δ_{B1} and δ_{B2} are the absolute errors between the estimated AOD and the reference AERONET observations. Best results are in boldface.

	AERONET		KF				Minimum			
	B1	B2	B1	B2	δ_{B1}	δ_{B2}	B1	B2	δ_{B1}	δ_{B2}
Chiang Mai	1.300	1.100	1.188	1.204	**0.112**	**0.104**	1.821	1.852	0.521	0.752

Table 8
RMSE, MAE, RMB are reported in this table for the four analyzed test cases in Colorado (USA) and Thailand. The analysis puts in evidence how the proposed Kalman filter (HEAD) approach improves the satellite retrieval based on the Minimum. Best results are in boldface.

	Date	KF			Minimum		
		RMSE	MAE	RMB	RMSE	MAE	RMB
CO	**2014-07-02**	**0.035**	**0.033**	**0.940**	0.240	0.240	0.160
	2014-08-12	**0.023**	**0.020**	**0.900**	0.088	0.082	0.390
Thai	**2014-03-20**	**0.140**	**0.140**	**1.060**	1.170	1.170	2.020
	2016-09-03	**0.110**	**0.110**	**1.010**	0.640	0.640	1.540

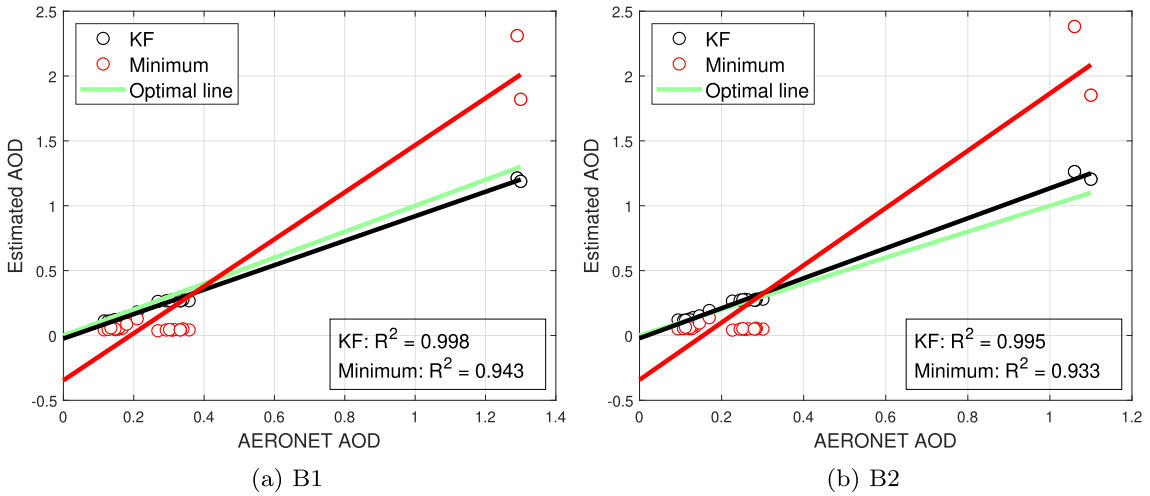

Fig. 10. AOD retrievals from the HEAD and the Minimum algorithms are validated against AERONET sun-photometer observations. Red dots refer to the Minimum measurements, instead, black dots are related to the HEAD. The solid lines are about the application of regression to measurements. The results show an improvement when HEAD (Kalman Filter; KF) is used. (For interpretation of the references to colour in this figure legend, the reader is referred to the web version of this article.)

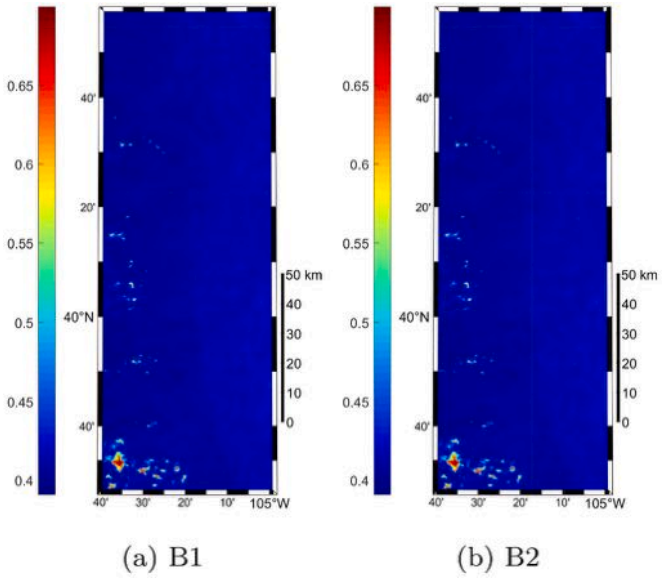

Fig. 11. Asymmetry parameter retrieval for B1 (coastal) and B2 (blue) bands, respectively, on 02 July 2014 in Boulder, Colorado (USA) region. (For interpretation of the references to colour in this figure legend, the reader is referred to the web version of this article.)

wild and remote regions. In-situ observations, despite a high temporal resolution, are sparse and not sufficient to characterize aerosol emissions at large scale. On other hand, the AOD, a comprehensive parameter directly related to the aerosol loading, is only available at a global scale exploiting satellite observations. In this work, we developed an algorithm based on Kalman filter to directly retrieve the AOD from high resolution multispectral satellite images in the blue wavelengths, independently on surface reflectance, aerosol type and without using look-up-tables or complex radiative transfer models. The proposed algorithm is important as it fills a gap to assess aerosol loading at regional scale. It has been tested for two different scenarios as in Colorado, during the NASA Discover-AQ campaign where a dense network of AERONET sunphotometer were deployed and taken as reference, and in Northern Thailand during intense biomass burning events. Despite the different scenarios, the inter-comparison put in evidence an excellent agreement between AERONET observational data and the algorithm retrieval. A further test case has also been presented showing the possibility of estimating (exploiting the proposed extended Kalman filter) the asymmetry factor parameter when AOD observations are available from ground-based stations. In future research, very high- resolution images will be used to provide AOD at 10 m resolution or finer.

Funding

ENVRI-FAIR has received funding from the European Union's Horizon 2020 research and innovation programme under grant agreement No 824068.

Declaration of Competing Interest

The authors declare that they have no known competing financial interests or personal relationships that could have appeared to influence the work reported in this paper.

References

Bar-Shalom, Y., Li, X.-R., 1995. Multitarget-multisensor Tracking: Principles and Techniques, vol. 19. YBs Storrs, CT.
Bilal, M., Nichol, J., Bleiweiss, M.P., Dubois, D., 2013. A simplified high resolution modis aerosol retrieval algorithm (sara) for use over mixed surfaces. Remote Sens. Environ. 136, 135–145.
Bilal, M., Nichol, J.E., Chan, P.W., 2014. Validation and accuracy assessment of a simplified aerosol retrieval algorithm (sara) over Beijing under low and high aerosol loadings and dust storms. Remote Sens. Environ. 153, 50–60.
Bilal, M., Qiu, Z., Campbell, J., Spak, S., Shen, X., Nazeer, M., 2018. A new modis c6 dark target and deep blue merged aerosol product on a 3 km spatial grid. Remote Sens. 10 (3), 463.
Bilal, M., Nazeer, M., Nicho, J.E., Bleiweiss, M.P., Qiu, Z., Jäkel, E., Campbell, J.R., Atique, L., Huang, X., Lolli, S., 2019. A simplified and robust surface reflectance estimation method (SREM) for use over diverse land surfaces using multi-sensor data. Remote Sens. 11 (11), 1–24.
Chudnovsky, A., Lyapustin, A., Wang, Y., Tang, C., Schwartz, J., Koutrakis, P., 2014. High resolution aerosol data from modis satellite for urban air quality studies. Open Geosci. 6 (1), 17–26.
Crawford, J.H., Pickering, K.E., 2014. Discover-aq: advancing strategies for air quality observations in the next decade. Environ. Manag. 4–7.
Deuzé, J., Bréon, F., Devaux, C., Goloub, P., Herman, M., Lafrance, B., Maignan, F., Marchand, A., Nadal, F., Perry, G., et al., 2001. Remote sensing of aerosols over land surfaces from polder-adeos-1 polarized measurements. J. Geophys. Res. Atmos. 106 (D5), 4913–4926.
Diner, D.J., Beckert, J.C., Reilly, T.H., Bruegge, C.J., Conel, J.E., Kahn, R.A., Martonchik, J.V., Ackerman, T.P., Davies, R., Gerstl, S.A., et al., 1998. Multi-angle imaging spectroradiometer (misr) instrument description and experiment overview. IEEE Trans. Geosci. Remote Sens. 36 (4), 1072–1087.
Diner, D.J., Davies, R., Kahn, R., Martonchik, J., Gaitley, B., Davis, A., 2006. Current and future advances in optical multiangle remote sensing of aerosols and clouds based on terra/misr experience. In: Remote Sensing of the Atmosphere and Clouds, Vol. 6408, International Society for Optics and Photonics, p. 640801.
Diner, D.J., Mischna, M., Chipman, R.A., Davis, A., Cairns, B., Davies, R., Kahn, R.A., Muller, J.-P., Torres, O., 2008. Windcam and mspi: two cloud and aerosol instrument concepts derived from terra/misr heritage. In: Earth Observing Systems XIII, Vol. 7081, International Society for Optics and Photonics, p. 70810T.
Giles, D.M., Sinyuk, A., Sorokin, M.G., Schafer, J.S., Smirnov, A., Slutsker, I., Eck, T.F., Holben, B.N., Lewis, J.R., Campbell, J.R., Welton, E.J., Korkin, S.V., Lyapustin, A.I., 2019. Advancements in the aerosol robotic network (aeronet) version 3 database – automated near-real-time quality control algorithm with improved cloud screening for sun photometer aerosol optical depth (aod) measurements. Atmos. Measur. Techniq. 12 (1), 169–209. https://doi.org/10.5194/amt-12-169-2019.
Grey, W.M., North, P.R., Los, S.O., Mitchell, R.M., 2006. Aerosol optical depth and land surface reflectance from multiangle aatsr measurements: global validation and intersensor comparisons. IEEE Trans. Geosci. Remote Sens. 44 (8), 2184–2197.
Griggs, M., 1975. Measurements of atmospheric aerosol optical thickness over water using Erts-1 data. J. Air Pollut. Control Assoc. 25 (6), 622–626.
Henyey, L.G., Greenstein, L.G., 1941. Diffuse radiation in the galaxy. Astrophys. J. 93, 70–83.
Holben, B., Vermote, E., Kaufman, Y.J., Tanré, D., Kalb, V., 1992. Aerosol retrieval over land from avhrr data-application for atmospheric correction. IEEE Trans. Geosci. Remote Sens. 30 (2), 212–222.
Holben, B., Eck, T., Slutsker, I., Tanré, D., Buis, J., Setzer, A., Vermote, E., Reagan, J., Kaufman, Y., Nakajima, T., Lavenu, F., Jankowiak, I., Smirnov, A., 1998. Aeronet—a federated instrument network and data archive for aerosol characterization. Remote Sens. Environ. 66 (1), 1–16.
Hsu, N.C., Tsay, S.-C., King, M.D., Herman, J.R., 2004. Aerosol properties over bright-reflecting source regions. IEEE Trans. Geosci. Remote Sens. 42 (3), 557–569.
Hsu, N.C., Tsay, S.-C., King, M.D., Herman, J.R., 2006. Deep blue retrievals of asian aerosol properties during ace-asia. IEEE Trans. Geosci. Remote Sens. 44 (11), 3180–3195.
Hsu, N.C., Li, C., Krotkov, N.A., Liang, Q., Yang, K., Tsay, S.-C., 2012. Rapid transpacific transport in autumn observed by the a-train satellites. J. Geophys. Res. Atmos. 117 (D6).
Hu, Y., Winker, D., Vaughan, M., Lin, B., Omar, A., Trepte, C., Flittner, D., Yang, P., Nasiri, S.L., Baum, B., et al., 2009. Calipso/caliop cloud phase discrimination algorithm. J. Atmos. Ocean. Technol. 26 (11), 2293–2309.
Kahn, R.A., Nelson, D.L., Garay, M.J., Levy, R.C., Bull, M.A., Diner, D.J., Martonchik, J.V., Paradise, S.R., Hansen, E.G., Remer, L.A., 2009. Misr aerosol product attributes and statistical comparisons with modis. IEEE Trans. Geosci. Remote Sens. 47 (12), 4095–4114.
Lepeule, J., Laden, F., Dockery, D., Schwartz, J., 2012. Chronic exposure to fine particles and mortality: an extended follow-up of the Harvard six cities study from 1974 to 2009. Environ. Health Perspect. 120 (7), 965–970.
Levy, R.C., Remer, L.A., Mattoo, S., Vermote, E.F., Kaufman, Y.J., 2007a. Second-generation operational algorithm: retrieval of aerosol properties over land from inversion of moderate resolution imaging spectroradiometer spectral reflectance. J. Geophys. Res. Atmos. 112 (D13).
Levy, R.C., Remer, L.A., Mattoo, S., Vermote, E.F., Kaufman, Y.J., 2007b. Second-generation operational algorithm: retrieval of aerosol properties over land from inversion of moderate resolution imaging spectroradiometer spectral reflectance. J. Geophys. Res. Atmos. 112 (D13).
Lolli, S., 2021. Is the air too polluted for outdoor activities? Check by using your photovoltaic system as an air-quality monitoring device. Sensors 21 (19). https://doi.org/10.3390/s21196342. https://www.mdpi.com/1424-8220/21/19/6342.
Lolli, S., Vivone, G., 2020. The role of tropospheric ozone in flagging covid-19 pandemic transmission. Bull. Atmos. Sci. Technol. 1–5.
Lolli, S., Delaval, A., Loth, C., Garnier, A., Flamant, P., 2013. 0.355-micrometer direct detection wind lidar under testing during a field campaign in consideration of esa's adm-aeolus mission. Atmos. Meas. Tech. 6, 3349–3358.
Lolli, S., Alparone, L., Garzelli, A., Vivone, G., 2017. Haze correction for contrast-based multispectral pansharpening. IEEE Geosci. Remote Sens. Lett. 14 (12), 2255–2259.
Lolli, S., Khor, W.Y., Matjafri, M.Z., Lim, H.S., 2019. Monsoon season quantitative assessment of biomass burning clear-sky aerosol radiative effect at surface by ground-based lidar observations in pulau pinang, Malaysia in 2014. Remote Sens. 11 (22).
Lolli, S., Chen, Y.-C., Wang, S.-H., Vivone, G., 2020. Impact of meteorological conditions and air pollution on covid-19 pandemic transmission in Italy. Sci. Rep. 10 (1), 1–15. https://doi.org/10.1038/s41598-020-73197-8.
Lyapustin, A., Martonchik, J., Wang, Y., Laszlo, I., Korkin, S., 2011. Multiangle implementation of atmospheric correction (Maiac): 1. Radiative transfer basis and look-up tables. J. Geophys. Res. Atmos. 116 (D3).
Lyapustin, A., Wang, Y., Korkin, S., Huang, D., 2018. Modis collection 6 Maiac algorithm. Atmos. Meas. Tech. 11 (10).
Miller, K.A., Siscovick, D.S., Sheppard, L., Shepherd, K., Sullivan, J.H., Anderson, G.L., Kaufman, J.D., 2007. Long-term exposure to air pollution and incidence of cardiovascular events in women. N. Engl. J. Med. 356 (5), 447–458.

Mülmenstädt, J., Feingold, G., 2018. The radiative forcing of aerosol–cloud interactions in liquid clouds: wrestling and embracing uncertainty. Curr. Clim. Change Rep. 4 (1), 23–40.
Omar, A., Winker, D., Tackett, J., Giles, D., Kar, J., Liu, Z., Vaughan, M., Powell, K., Trepte, C., 2013. Caliop and aeronet aerosol optical depth comparisons: one size fits none. J. Geophys. Res. Atmos. 118 (10), 4748–4766.
Ouaidrari, H., Vermote, E.F., 1999. Operational atmospheric correction of landsat tm data. Remote Sens. Environ. 70 (1), 4–15.
Remer, L.A., Kaufman, Y., Tanré, D., Mattoo, S., Chu, D., Martins, J.V., Li, R.-R., Ichoku, C., Levy, R., Kleidman, R., et al., 2005. The modis aerosol algorithm, products, and validation. J. Atmos. Sci. 62 (4), 947–973.
Sayer, A., Smirnov, A., Hsu, N., Holben, B., 2012a. A pure marine aerosol model, for use in remote sensing applications. J. Geophys. Res. Atmos. 117 (D5).
Sayer, A., Hsu, N., Bettenhausen, C., Ahmad, Z., Holben, B., Smirnov, A., Thomas, G., Zhang, J., 2012b. Seawifs ocean aerosol retrieval (soar): algorithm, validation, and comparison with other data sets. J. Geophys. Res. Atmos. 117 (D3).
She, L., Zhang, H., Wang, W., Wang, Y., Shi, Y., 2019. Evaluation of the multi-angle implementation of atmospheric correction (Maiac) aerosol algorithm for himawari-8 data. Remote Sens. 11 (23) https://doi.org/10.3390/rs11232771. https://www.mdpi.com/2072-4292/11/23/2771.
Stow, D.A., Chen, D.M., 2002. Sensitivity of multitemporal noaa avhrr data of an urbanizing region to land-use/land-cover changes and misregistration. Remote Sens. Environ. 80 (2), 297–307.
Tanré, D., Bréon, F., Deuzé, J., Dubovik, O., Ducos, F., François, P., Goloub, P., Herman, M., Lifermann, A., Waquet, F., 2011. Remote sensing of aerosols by using polarized, directional and spectral measurements within the a-train: the parasol mission. Atmos. Meas. Tech. Discuss. 4, 2037–2069.
Thomas, G., Poulsen, C., Sayer, A., Marsh, S., Dean, S., Carboni, E., Siddans, R., Grainger, R., Lawrence, B.N., 2009. The grape aerosol retrieval algorithm. Atmos. Measur. Techniq. Discuss. 2 (2).
Tosca, M.G., Campbell, J., Garay, M., Lolli, S., Seidel, F.C., Marquis, J., Kalashnikova, O., 2017. Attributing accelerated summertime warming in the Southeast United States to recent reductions in aerosol burden: indications from vertically-resolved observations. Remote Sens. 9 (7), 1–17.
Toth, T.D., Zhang, J., Reid, J.S., Vaughan, M.A., 2019. A bulk-mass-modeling-based method for retrieving particulate matter pollution using caliop observations. Atmos. Measur. Techniq. 12, 1739.
Van Donkelaar, A., Martin, R.V., Park, R.J., 2006. Estimating ground-level pm2. 5 using aerosol optical depth determined from satellite remote sensing. J. Geophys. Res. Atmos. 111 (D21).
Vaughn, M., Powell, K., Winker, D., Hostetler, C., Kuehn, R., Hunt, W., Getzewichand, B., Young, S., Liu, Z., McGill, M., 2009. Fully automated detection of cloud and aerosol layers in the calipso lidar measurements. J. Atmos. Ocean. Technol. 26, 2034–2050.
Vermote, E., Justice, C., Claverie, M., Franch, B., 2016. Preliminary analysis of the performance of the landsat 8/oli land surface reflectance product. Remote Sens. Environ. 185, 46–56.
Vivone, G., Restaino, R., Chanussot, J., 2018a. Full scale regression-based injection coefficients for panchromatic sharpening. IEEE Trans. Image Process. 27 (7), 3418–3431.
Vivone, G., Restaino, R., Chanussot, J., 2018b. A bayesian procedure for full resolution quality assessment of pansharpened products. IEEE Trans. Geosci. Remote Sens. 56 (8), 4820–4834.
Wong, M.S., Nichol, J.E., Lee, K.H., 2011. An operational modis aerosol retrieval algorithm at high spatial resolution, and its application over a complex urban region. Atmos. Res. 99 (3–4), 579–589.
Zhao, F., Li, Y., Dong, C., Lu, N., 2002. An algorithm for determination of aerosol opticalthickness from avhrr imagery over oceans. Meteorog. Atmos. Phys. 80 (1–4), 73–88.